Monthly Notices of the ROYAL ASTRONOMICAL SOCIETY

MNRAS **528,** 909–918 (2024)
Advance Access publication 2023 December 20

https://doi.org/10.1093/mnras/stad3928

He abundance in NGC 1850 A and B: Are we observing the early stage of the formation of multiple populations in a stellar cluster? ★

R. Carini [1]★ A. Sollima [2] E. Brocato [1,3] and K. Biazzo [1]

[1] *INAF – Osservatorio Astronomioco di Roma (OAR), via Frascati 33, 00078 Monte Porzio Catone (RM), Italy*
[2] *INAF – Osservatorio di Astrofisica e Scienza dello Spazio (OAS), via Giobetti 93/3, 40129 Bologna, Italy*
[3] *INAF – Osservatorio Astronomico d'Abruzzo, via M. Maggini snc, I-64100 Teramo, Italy*

Accepted 2023 December 15. Received 2023 December 15; in original form 2023 July 30

ABSTRACT

We present the results for a sample of B stars in the Large Magellanic Cloud young double stellar cluster NGC 1850 A and NGC 1850 B, as observed with the integral-field spectrograph at the Very Large Telescope, the Multi Unit Spectroscopic Explorer (MUSE). We compare the observed equivalent widths (EWs) of four He lines (4922, 5015, 6678, and 7065 Å) with those determined from synthetic spectra computed with different He mass fractions ($Y = 0.25$, 0.27, 0.30, and 0.35) with the code SYNSPEC, which takes into account the non-local thermodynamic equilibrium effect. From this comparison, we determine the He mass fraction of the B stars, finding a distribution that is not homogeneous. The stars can be divided in three groups: He-weak ($Y < 0.24$) and He-normal ($0.24 \leq Y \leq 0.26$) stars, belonging to the main sequence of NGC 1850 A, and He-rich stars ($0.33 \leq Y \leq 0.38$), situated in the main sequence associated with NGC 1850 B. We analyse the stellar rotation as possibly being responsible for the anomalous features of the He lines in the He-rich stars. We provide a simple analysis of the differences between the observed EWs and those obtained from theoretical models with different rotation velocities ($V\sin i = 0$ and 250 km s^{-1}). The resolution of the MUSE spectra does not allow us to obtain a conclusive result; however, our analysis support the He-enhanced hypothesis.

Key words: methods:observational – technique: spectroscopic – stars: abundances –galaxies:star clusters: individual: NGC 1850.

1 INTRODUCTION

NGC 1850 is a young ($t_{age} \sim 90$ Myr; Niederhofer et al. 2015) and massive ($M \sim 5.5 \times 10^4$ M$_\odot$; Fischer, Welch & Mateo 1993) stellar cluster in the Large Magellanic Cloud (LMC), located at the edge of the galaxy bar. The cluster appears to be a binary system (NGC 1850 A and NGC 1850 B), and there is an indication of tidal interaction between the system members (Fischer, Welch & Mateo 1993). NGC 1850 B is located ∼30 arcmin west of the main cluster, constitutes ∼2 per cent of the total cluster population, and is characterized by a significantly younger age (between 4 and 15 Myr; Fischer, Welch & Mateo 1993; Gilmozzi et al. 1994; Vallenari et al. 1994; Sollima et al. 2022). The colour–magnitude diagram (CMD) of NGC 1850 A reveals a main sequence turn-off (MSTO) region that is wider than what is expected from a single stellar population and that shows the presence of two main sequences (MSs): a blue and poorly populated MS, and a red MS that contains the majority of the stars. These features are not compatible with the typical photometric uncertainties, such as field star contamination and differential reddening (Bastian et al. 2016; Correnti et al. 2017; Milone et al. 2018).

A split of the MS and extended-MSTO (eMSTO) have been observed in many young (age less than 800 Myr and ∼2.5 Gyr respectively) massive star clusters (YMCs) in the Magellanic Clouds (MCs) (Milone et al. 2023). Unlike Galactic globular clusters (GGCs), in which the observational evidence for multiple populations is mainly provided by star-to-star chemical abundance variations (e.g. He, Na, O; see reviews by Bastian & Lardo 2018 and Gratton et al. 2019; Milone & Marino 2022 and references therein), the YMCs of the MCs appears chemically homogeneous (e.g. Mucciarelli et al. 2014; Milone et al. 2020). The origin of the eMSTOs and the split MSs is still being debated. In early works, the eMSTO was interpreted as the result of a prolonged period of star formation (e.g. Mackey et al. 2008; Keller, Mackey & Da Costa 2011). Now, stellar rotation has been suggested as the dominant cause of these photometric features (Bastian & de Mink 2009; D'Antona et al. 2015); however, rotation effects do not fully reproduce the observed MSTOs of the entire sample of the CMD observed in the MCs (e.g Milone et al. 2017). As a consequence, some authors suggest that a mix of age variation and rotation could explain the eMSTOs and split-MS phenomena in a more effective way (Goudfrooij, Girardi & Correnti 2017; Costa et al. 2019). In the case of NGC 1850, Correnti et al. (2017) suggested that the combination of single stellar populations (SSPs) with an age range of ∼35 Myr along with different rotation

★ This paper is dedicated to the memory of Dr Antonio Sollima, who passed away prematurely in 2023.

★ E-mail: roberta.carini@inaf.it

rates could explain explain the eMSTO and the MS split of the cluster.

Recently, Kamann et al. (2023) found rotation velocity differences along the blue and red MSs, with the blue arm consisting primarily of slow rotators (~ 100 km s^{-1}), and the red arm consisting mainly of rapid rotators (~ 200 km s^{-1}). At present, the phenomena of multiple stellar populations in YMCs and in GGCs seem not to share the same origin and cause.

If the hypothesis of a dynamical association between NGC 1850 A and NGC 1850 B is adopted, this binary cluster seems to have the right mass and size to evolve in the next 10 Gyr towards the typical configuration of a present-day GC formed by two distinct stellar populations (Baumgardt & Hilker 2018). Thus, the intriguing possibility exists that this cluster could serve as a unique bridge between the young massive stellar clusters observed during the formation of multiple populations and the GCs exhibiting multiple populations observed some Gyr after their formation. Therefore, with the aim of better understanding the stellar populations in YMCs and their possible evolution towards a GC appearance, we analyse the chemical abundance in NGC 1850 A and NGC 1850 B.

The presence of He spread has been the main marker of multiple populations in GCs (eg. Cassisi et al. 2017; Gratton et al. 2019; Milone & Marino 2022 and reference therein). All formation scenarios aiming to explain the origin of multiple populations in GCs predict that the second generation of stars are enhanced in He. The difference in He abundance between stellar populations can explain the peculiarities in the CMDs of the GGCs, such as the MS split and the morphology of the horizontal branch (see review by Bastian & Lardo 2018; Gratton et al. 2019; Milone & Marino 2022 and references therein). In fact, owing the higher molecular weight, stars with higher abundances of He evolve more rapidly and are more luminous than lower-He models of the same mass, so the sequence of the He-rich models is bluer. Moreover, different scenarios predict quite different He abundances at the end of the formation processes. For example, in the AGB (asymptotic giant branch) scenario, the maximum He enhancement expected is of the order of 0.36–0.38 in terms of the mass fraction (Siess 2010; Doherty et al. 2014); in contrast, the fast-rotating massive star scenario predicts He values up to ~0.8 (Chantereau, Charbonnel & Meynet 2016). Therefore, the He abundance is clearly crucial to constrain the origin of the multiple populations. The first direct spectroscopic measurement of highly He-enhanced stars ($Y \sim 0.34$) was provided by Marino et al. (2014), who analysed the blue horizontal branch of the GGC NGC 2808.

Although He is the second most abundant element in stars, estimates of He abundance in stellar clusters are quite rare. Recently, Lagioia et al. (2019) found traces of He enhancement ($\delta Y \sim 0.01$) in the second population of stars of four GCs belonging to the SMC and showing ages in the range of ~6−10 Gyr. Carini et al. (2020) estimated the He abundance of 10 star in the stellar cluster NGC 330 in the SMC, finding a mean value of $\langle\epsilon(\mathrm{He})\rangle = 10.93 \pm 0.05$, without evidence of star-to-star He abundance difference. Li et al. (2023) found an He spread of $\delta Y \sim 0.06$–0.07 in the MS dwarf stars in the old GC NGC 2110, in the LMC. We intend to tackle this puzzling scenario by evaluating the He abundance in NGC 1850 A and B. In particular, we analyse the He abundance in B-type stars, whose visible spectra are dominated by lines of He I and the Balmer series of hydrogen. These are rather hot, massive stars with effective temperatures in the range from 1.0×10^4 to 3.0×10^4 K and masses in the range from 2 to 20 $M_\odot$.

Here, we continue the line of research of Sollima et al. (2022), using the same set of data observed with the Multi Unit Spectroscopic Explorer (MUSE) integral field spectrograph in adaptive optics mode and the photometric parameters found by the authors during their analysis.

This paper is organized as follows. In Section 2 we describe the MUSE observations and data reduction, while the synthetic spectra are illustrated in Section 3. The data analysis, the determination of the He abundance, the associated uncertainties, and the influence of stellar rotation on the He features are presented in Section 4. Some final remarks are provided in the last section.

2 OBSERVATIONS

We analysed a set of cubes observed with the integral field spectrograph of MUSE (Bacon et al. 2010; Kelz et al. 2016) at the Very Large Telescope (VLT) under the observing program 0102.D-0268(A) (PI: Bastian). Observations were conducted over a period of 6 nights between 2019 January and March. Two fields were observed during each visit, namely a central field located at the cluster centre (exposure time $t_{\rm exp} = 2 \times 400$ s) and an outer field ($t_{\rm exp} = 3 \times 500$ s), approximately 1 arcmin south-east of the cluster centre, with a small overlap with the central field. The total exposure time per visit was 2300 s. The data were obtained using the wide-field mode, with the ground-layer adaptive optics system activated. Each field of view was of 1×1 arcmin^2, with a spatial sampling of 0.2 arcsec. The wavelength range covered by the instrument is $\lambda = 4800$–9300 Å, with a low-to-medium resolution ($R \sim 1700$–3500). Owing to the emission of the laser guide star, the portion of the spectrum between 5805 and 5965 Å has been masked. We downloaded the cubes reduced from the ESO Archive Science Portal.[1] The six data cubes, containing flux and a wavelength-calibrated spectrum in each spaxel, cover NGC 1850 A and B, both visible at the right edge of the central point. Moreover, the combined cube was available. This data set has already been used to determine the binary frequency on each of the arms of the split MS (Kamann et al. 2021) as well as to study the peculiar system NGC 1850-BH1 (El-Badry & Burdge 2022; Saracino et al. 2022) and the effect of the shell stars on the shape of the MSTO (Kamann et al. 2023). Sollima et al. (2022) determined the global metallicity on the basis of individual red supergiant (RSG) spectra ($<[M/H]> = -0.31 \pm 0.01$), the Ba abundances ($<$[Ba/Fe]$> = 0.4 \pm 0.02$), and the dynamical mass ($\log(M/M_\odot) = 4.84 \pm 0.10$) of the cluster. Moreover, the authors analysed the O abundance among bright MS stars in NGC 1850. They found two groups of stars: the O-strong stars ([O=Fe] = –0.16 ± 0.05) agree with the value measured in stars with a similar metallicity in the LMC bar (Van der Swaelmen et al. 2013), and the O-weak stars display no O I triplet absorption lines. The authors interpreted this bimodality as evidence for different stellar rotation rates.

3 SYNTHETIC SPECTRA

In order to analyse the B-star spectra, we computed detailed synthetic spectra with SYNSPEC version 54 (Hubeny et al. 2021) using non-local thermodynamic equilibrium (non-LTE) line-blanketed, model atmospheres of the grid *BSTAR*2006 (Lanz & Hubeny 2007) for early B stars. We chose the non-LTE approach because many authors (e.g. Auer & Mihalas 1973; Przybilla et al. 2005, 2006) have shown in their analyses how the LTE approach leads to an erroneous abundance of He in B stars. The model atmospheres, calculated with TLUSTY (Lanz & Hubeny 2007), consider a 1D plane–parallel geometry, with hydrostatic and radiative equilibrium. The grid contains 16 effective

[1] http://archive.eso.org/scienceportal/home

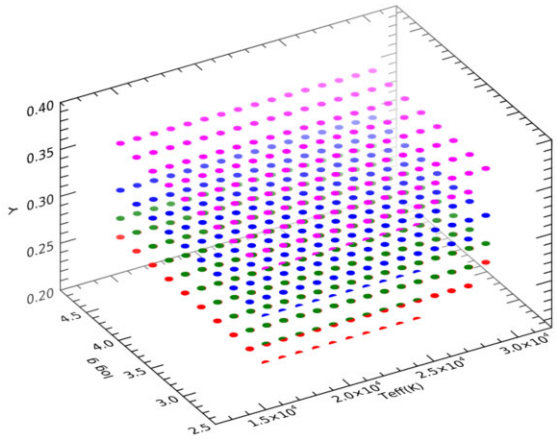

Figure 1. Grid points in the log g versus T_{eff} versus Y plan. Red, green, blue, and magenta dots represent different He mass fractions of $Y = 0.25$, 0.27, 0.30, and 0.35 respectively. For a colour version of the figure, see the electronic version of the paper.

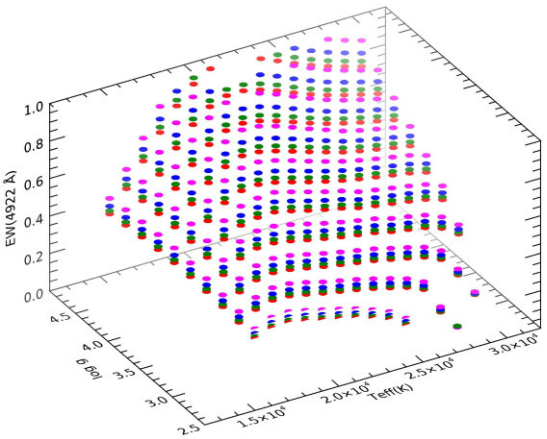

Figure 2. Equivalent width of the 4922-Å line in the log g versus $T_{\rm eff}$ versus Y plan. The symbols are as in Fig. 1.

temperatures, 15 000 K $\leq T_{\rm eff} \leq$ 30 000 K with 1000-K steps, 10 surface gravities, 2.50 $\leq \log g \leq$ 4.75 with 0.25-dex steps, and 10 metallicities: 2, 1, 1/2, 1/5, 1/10, 1/30, 1/50, 1/100, 1/1000, and 0 times the solar metal composition. The grid is thus useful for studies of the typical environments of massive stars: the Galactic Centre, the MCs, blue compact dwarf galaxies such as I Zw-18, and galaxies at high redshifts. For model atmospheres, the grid is available on the TLUSTY website.[2] Considering the typical characteristics of the star of NGC 1850, we adopt stellar atmospheric models with $Z = 0.008$ and a microturbulent velocity of 2 km s^{-1}. In fact, recent studies have determined the metallicity of the cluster: Sollima et al. (2022) and Song et al. (2021) found a value [M/H] = –0.31 ($Z \sim 0.008$), and Kamann et al. (2023) found –0.33. The standard solar abundances adopted are those by Asplund, Grevesse & Sauval (2005).

The model atmospheres explicitly include, and allow for departures from LTE, 46 ions of H, He, C, N, O, Ne, Mg, Al, Si, S, and Fe, and about 53 000 individual atomic levels grouped into 1127 superlevels. For more details, see Lanz & Hubeny (2007), Hubeny et al. (2021) and reference therein. The triplet lines of He at 4922 Å are treated using special line broadening tables, in accordance with Barnard, Cooper & Smith (1974) and Shamey (1969).

To have He-enhanced synthetic spectra, it is not advantageous to construct a model from scratch, so we used the existing model from the grid to interpolate the values for the required He abundance. A conservative estimate is to change the chemical abundance by no more than 0.2 dex (Hubeny & Lanz 2017b). Because the difference in He abundance between the populations could range from less than 0.01 to more than 0.2 in He mass fraction (Y) (e.g. D'Antona & Caloi 2004, Milone 2015, Gratton et al. 2019, Milone & Marino 2022 and reference therein), for each of these combinations in $T_{\rm eff}$–log g, models with a He abundance of log$N$(He)/N(H)= 0.00, +0.04, +0.1, and +0.2 dex were computed, corresponding to a He abundance with a mass fraction of $Y = 0.25$, 0.27, 0.30 and 0.35.

The whole set of grid points are shown in Fig. 1, in the log g versus $T_{\rm eff}$ versus Y plan.

To obtain a synthetic spectrum that is directly comparable to observations, it is necessary to convolve the net emergent flux with the instrumental profile of the spectrograph that produced the observed spectrum to be analysed. To this end, the synthetic spectra were degraded at the MUSE resolution and normalized with the ROTIN code (Hubeny & Lanz 2017a). For each spectrum, we determined the equivalent width (EW) of four He absorption lines, at 4922, 5015, 6678, and 7065 Å. We omitted the most intensive He line, at 5876 Å, because it is not available in the MUSE spectra, as it falls in the portion of the spectrum that is masked. We obtained these values numerically, integrating the normalized spectrum considering a 10-Å-wide region on both sides of the He I lines. As an example, in Fig. 2 we show the EW of the 4922-Å line, calculated from the synthetic spectra.

As shown in Fig. 2, the behaviour of the intensity of the EW is in agreement with the theory. As expected:

(i) the EWs increase with the He abundance;
(ii) because lines of neutral He first show up in O-type stars, strengthen through the O-type stars, come to a maximum at spectral type B2 on the MS, and the weaken towards later (cooler) types, the behaviour of the EWs has a maximum at 16 000–22 000 K, and decreases for cooler and hotter temperatures;
(iii) the intensity of the lines increases with the surface gravity.

Moreover, for values of $T_{\rm eff}$ less than 17 000 K, the strengths of this line are quite sensitive to temperature but relatively insensitive to gravity. For $T_{\rm eff}$ between 18 000 and 22 000 K, the abundance is dependent on log g more than on $T_{\rm eff}$. At still higher temperatures, both $T_{\rm eff}$ and log g must be accurately determined in order to derive the abundance of He from the measured EWs (Wolff & Heasley 1985).

To compare the theoretical equivalent width (EW_{th}) with the observed ones (EW_{obs}), we interpolated through the non-LTE grid of synthetic EWs as a function of $T_{\rm eff}$ and log g.

4 DATA ANALYSIS

Spectra were extracted from the final MUSE data cubes using software specifically developed by Sollima et al. (2022; for details see part 2 of the paper). The extraction was performed on each individual data cube, including the combined cube ($cube_{sum}$ hereafter). We extracted the spectra of the same 1167 stars from each cube. Residuals from the strong nebula emission lines are still visible in some of the extracted spectra, but they do not affect the He lines. The region analysed is not heavily influenced by nebularity. In fact, by analysing the spectra of the background in regions near our selected stars,

[2] http://tlusty.oca.eu/Tlusty2002/tlusty-frames-BS06.html

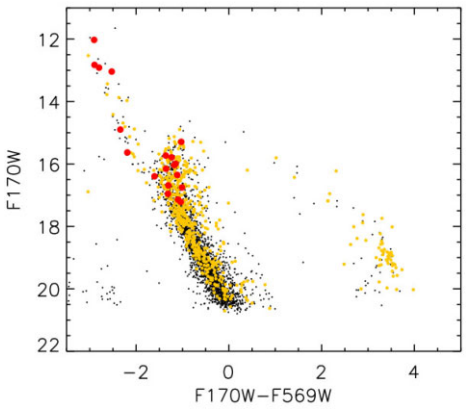

Figure 3. Colour-magnitude diagram of the stars in the NGC 1850 area. Black dots are the *HST* data, yellow dots are the stars extracted from the MUSE data cube, and the red circles are the B stars analysed here, for which we have determined the He abundance.

we verified the absence of He lines in emission. To identify the MUSE targets and to determine their effective temperature ($T_{\rm eff}$) and gravity ($\log g$), we used the archival *Hubble Space Telescope* (*HST*) photometry of NGC 1850 taken with the Wide Filed Planetry Camera 2 (WFPC2) on 1994 March 4, during program #5559 (PI: Gilmozzi). The data, reduced using DOLPHOT software (Dolphin 2000), include the images taken in three filters, F170W, F439W and F569W, and have been presented in Gilmozzi et al. (1994) and Sollima et al. (2022).

In Fig. 3, we show the CMD in the F170W and F569W bands. The black dots are the *HST* data, the yellow ones represent the MUSE targets extracted, and the red ones are the B stars selected to estimate the He abundance (see Section 4.1). The MUSE sample covers a wide range of colour and magnitude, and it is possible recognize the blue supergiants of NGC 1850 B (F170W – F569W < -2) and the MS, RG, and blue loop stars of NGC 1850 A (F170W – F569W > -2). Contamination from LMC stars is also present (F439W – F569W > 0.3 and F569W > 17; the magnitude in the band F170W of these targets is not given in the catalogue). Relevant quantities of selected stars of our sample (see Section 4.1) are reported in Table 1; they were determined by comparing them with appropriate theoretical isochrones (see Sollima et al. 2022 for more details about this technique). We used Marigo et al.'s (2008) set of solar-scaled isochrones with a metallicity of $Z = 0.008$ and ages of 15 Myr, 90 Myr, and 10 Gyr. Stars with the colour F170W − F569W < -2 or stars within 5 arcmin from the centre of the cluster NGC 1850 B to the youngest one, stars belong to NGC 1850 A are fitted with the isochrone at 90 Myr, and stars of the LMC are associated with the oldest isochrone. The distance modulus $(m - M)_0 = 18.50$ (Niederhofer et al. 2015) and the reddening $E(B - V) = 0.13$ (Górski et al. 2020) were adopted. Once $T_{\rm eff}$ and $\log g$ were determined, the radial velocities of the targets stars were derived by cross-correlating the stellar spectra with the appropriate and previously calculated synthetic spectra. Cross-correlation was performed using the *fxcorr* task from IRAF, considering the available He lines. As noted by Sollima et al. (2022), the accuracy of the radial velocity varies greatly with the colour of the targets: for this reason, the values found for the B stars in this work are slightly different from the average velocities found by Sollima et al. (2022), Fischer, Welch & Mateo (1993) (251.4 ± 2 km s^{-1}) and Song et al. (2021) (248.9 ± 2.5 km s^{-1}), who derived the radial velocity from a sample of RSG stars that are much cooler than the stars used here. Finally, we shifted the spectra to the rest frame.

Table 1. Relevant quantities of the stars of our selected sample.

ID	RA	Dec.	$T_{\rm eff}$ (K)	Log g (dex)	$v_{\rm rad}$ (km s^{-1})	$\sigma_{v_{\rm rad}}$ (km s^{-1})
		NGC 1850 A				
222	77.2163239	−68.7669383	15 200	4.16	270	8
377	77.2080954	−68.7678015	15 000	4.10	266	8
415	77.206	−68.761	20 300	4.27	270	7
511	77.2018423	−68.7656164	16 100	3.85	285	5
564	77.1990042	−68.7531787	17 900	3.98	267	10
727	77.1924089	−68.7728569	16 600	4.15	261	17
753	77.1915224	−68.7681341	15 700	4.16	255	10
907	77.185	−68.774	16 800	3.92	275	10
952	77.1835724	−68.7753472	16 600	4.10	259	9
971	77.1830299	−68.770169	15 800	3.98	280	11
1036	77.1795715	−68.7560604	15 100	3.34	266	9
1069	77.1767874	−68.761876	16 000	3.85	253	8
1129	77.1703261	−68.7598117	16 800	3.77	235	7
		NGC 1850 B				
605	77.1974417	−68.7680385	21 400	4.27	254	6
1020	77.1805277	−68.7682749	25 100	3.94	261	10
1077	77.1760504	−68.7641924	23 000	4.20	257	9
1146	77.1673117	−68.7613749	29 900	3.83	255	10
1153	77.1655824	−68.7616053	30 000	3.62	262	8
1160	77.1639984	−68.7606044	28 500	3.83	257	10
1161	77.1635335	−68.7617016	25 800	3.83	269	8

4.1 Selection criteria for our sample of B stars in NGC 1850 A and NGC 1850 B

On the basis of the 1167 stars in our sample of MUSE spectra, we selected the stars with a $T_{\rm eff}$ between 15 000 and 30 000 K, and surface gravity $\log g$ between 2.5 and 4.75, values of the theoretical grid (see Section 3). We also selected stars with at least two available measurements of magnitude in the bands F170W, F439W and F569: this is to secure a fairly reliable determination of the $T_{\rm eff}$ for the stars included in the selected sample. In this way, we ended up with a sample reduced to 232 targets.

Moreover, we excluded Be stars to minimize uncertainties due to rotation and complexity in the spectral analysis; these were were identified spectroscopically through the Hα emission. We found a fraction of Be stars that was slightly higher (∼65 per cent of the sample) than that found in NGC 1850 by Bastian et al. (2017) (∼20–50 per cent) and in other young massive clusters (Milone et al. 2018) (40–55 per cent).

We also excluded spectra showing stellar activity, those in which the He lines are too faint to be fitted, and those in which the signal-to-noise ratio (S/N) is lower than 30. Finally, our selected simple is composed of 20 B stars, and all these stars are shown as red circles in Fig. 3. This sample includes B stars of NGC 1850 A and B as reported in Table 1. For simplicity, we consider stars of NGC 1850 B each target associated to the youngest isochrone, even if the distance from the centre of the subcluster is more than 5 arcmin.

4.2 He abundance

In this section, we make use of the spectral data secured by MUSE observations to evaluate the He abundances in the B stars of NGC 1850 A and B, and to investigate the presence of a possible spread of this quantity in our sample.

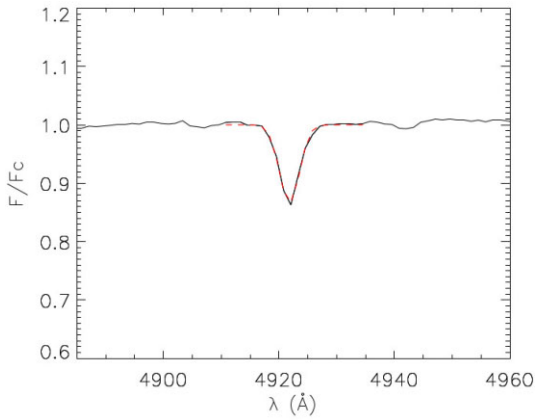

Figure 4. Best fit of the He line at 4922 Å for star #1146. The black line is the part of the spectrum extracted near the line, and the red dashed line is the best fit.

4.2.1 ***EW determination***

To estimate the He abundance, we determined the EW of the lines at 4922, 5015, 6678, and 7065 Å from the observed spectra. These values were then compared with the theoretical ones.

For the middle B spectral types, the interpretation of He I at 4921.9 Å is complicated by the blends with Si II at λ 4921.7 Å and with lines of Fe II and S II at λ 4923.9 Å, while for B0 and B1, O II lines at λ 4924.6 Å perturbs the red wing of He I λ 4921.9 Å. Moreover, middle and late B spectra are affected by S II at λ 5014.0 Å blending with He I at λ 5015.7 Å (Leckrone 1971). All these issues are well known; nevertheless, we recall them to emphasize that the evaluation of He abundances in this range of wavelengths has to be conducted with special care. For this reason, our results will be used to highlight qualitative new discoveries, which will lead to further work for quantitative confirmation.

In this work, each He line was fitted individually to derive the EWs. As a first step, the continuum was estimated via a linear fit of the flux obtained in two narrow ranges (10 Å) of wavelength near the wings of each He absorbing line we intend to evaluate. This local continuum was used to normalize the part of the spectra where the He line is present.

The previous step makes it possible to evaluate the EW of each He line by performing a Gaussian fit. As an example of the good quality of this step, Fig. 4 shows the best fit (red dashed line) obtained for star #1146 at 4922 Å.

Unfortunately, the strongest line at 5876 Å was not taken into account because the section of the He line near the sodium doublet was masked to avoid the strong emission due to the laser guide. It is relevant to report that none of these stars, except #971, exhibit a significant variation in radial velocity or in the EW values among the six epochs. This means that the stars of our sample can be considered as single stars, or their companion is a low-mass star that does not significantly affect the radial systemic velocity. Because the S/N in the cube_{sum} is systematically higher than the S/N found in each single cube, and the values of the mean EWs of each line of the single cubes are in agreement, within the error, with the EW values of the cube_{sum}, we decided to continue the analysis with only the values estimated from the last one. In Table 2, we present the EWs of the He lines at 4922, 5015, 6678, and 7065 Å. Empty cells in this table refer to features for which the best fit was not obtained, in most cases because the observed line was too weak or not detectable in the noise. In Fig. 5 we show the EW_{obs} (black dots) for each star in each He I line as a function of temperature in comparison with those calculated with a different He mass fraction, $Y = 0.25$ (red asterisks) and $Y = 0.35$ (blue diamonds). For the sake of clarity, the plot does not include the EW_{th} relative to $Y = 0.27$ and $Y = 0.30$. This figure shows quite a good agreement between the trend of the EW_{th} and that of EW_{obs} as a function of T_{eff}. This result supports our previous assumption about the non-LTE, which appears to be the most appropriate to analyse the He abundance in B stars.

4.2.2 He mass fraction evaluation

An evaluation of the He mass fraction (Y) from the EW_{obs} of the He lines can be obtained using the synthetic computed for these lines. For this purpose, we used a non-LTE grid of EW_{th} covering a wide range of effective temperature and gravity. The precise values of Y are then obtained by accurate interpolations through the non-LTE grid of EW_{th} for each line as a function of gravity, temperature, and He, when the measured quantities (EW_{obs}) are within the border values of the grid. In case the value is outside the available grid, we obtain a fair evaluation of the Y by using a linear extrapolation. We show an example of both cases in Fig. 6 for star #1146. The cyan square is the measured EW from the MUSE spectrum, while the black circles are the values of the synthetic EWs corresponding to $Y = 0.25$, 0.27, 0.30 and 0.35. The red lines represent the linear fit of the synthetic data.

Finally, we derived the He abundance by computing the mean of the abundances found for each available line: the results are reported in column 6 of Table 2 with the associated standard deviation (column 7). It is evident from our analysis that we can divide our sample into three groups: *He- normal* stars, *He- weak* stars, and *He-enhanced*, or *He-rich*, stars. Even if the typical He mass fraction value for LMC stars is $Y = 0.25$, considering the uncertainties in the determination of the He abundance, we call *He-normal* stars the targets with Y between 0.24 and 0.26. The second group is populated by targets showing $Y < 0.24$, while the third is the sample containing the stars with $Y > 0.26$.

We plot the targets of the three groups in the CMD with different symbols (Fig. 7). It is evident that they are located in specific parts of the CMD, as follows.

(i) *He-rich* stars, with the exception of the target #1069, are located in the region of the MS associated with the isochrone at 15 Myr, with which we identify the NGC 1850 B cluster;

(ii) Most of the *He-normal* stars (green diamonds) have a F170W magnitude larger than –2 mag; they are present only in the MS that collects the stars belonging to NGC 1850 A.

(iii) The *He-weak* stars (light blue squares) seem to populate the reddest part of the MS (F170W lower than –2 mag).

According to Osawa (1965) and Garrison & Gray (1994), it is not surprising to find He-weak stars, because they constitute a subclass of B-type stars. The He-weak stars have effective temperatures of typical B3–B5 stars, as in our subsample, and the weak He lines in the spectra of certain stars cause their spectral types to be inaccurately determined, leading to a discrepancy between their spectral type and their apparent colour. Moreover, there is evidence that their spectra show variations in the metal lines and perhaps He lines (Molnar 1972), as could be the case for target #197 of our sample.

The He-rich targets (red circles) are in the hot and bright part of the CMD, that is, where the younger stars are located and in the region where we identify most of the stars of NGC 1850 B. On average, the Y value of these stars is 0.35 ± 0.02.

Table 2. Equivalent width (in Å) obtained from our analysis for each line and the derived mean He abundance (Y).

Star	EW (λ4921.9 Å)	EW (λ5015.7 Å)	EW (λ6678.2 Å)	EW (λ7065.7 Å)	$<Y>$	$\sigma(Y)$
			NGC 1850 A			
222	0.40 ± 0.04	0.19 ± 0.04	...	...	0.24	0.02
377	0.46 ± 0.04	0.17 ± 0.04	...	...	0.25	0.10
415	0.87 ± 0.07	...	0.52 ± 0.60	0.34 ± 0.06	0.26	0.01
511	0.39 ± 0.03	0.22 ± 0.04	0.30 ± 0.02	0.19 ± 0.03	0.20	0.05
564	0.63 ± 0.04	0.32 ± 0.02	0.43 ± 0.03	0.25 ± 0.04	0.24	0.08
727	0.52 ± 0.02	0.20 ± 0.04	0.40 ± 0.03	...	0.25	0.11
753	0.31 ± 0.06	...	0.22 ± 0.04	0.18 ± 0.04	0.18	0.10
907	0.41 ± 0.03	0.22 ± 0.03	0.26 ± 0.02	0.17 ± 0.02	0.10	0.06
952	0.52 ± 0.03	0.25 ± 0.08	...	...	0.26	0.06
971	0.33 ± 0.02	0.18 ± 0.06	...	...	0.13	0.06
1036	0.35 ± 0.02	0.20 ± 0.02	0.23 ± 0.01	...	0.16	0.06
1069	0.51 ± 0.04	0.25 ± 0.02	0.26 ± 0.02	0.23 ± 0.02	0.27	0.08
1129	0.52 ± 0.04	0.24 ± 0.06	...	...	0.22	0.02
			NGC 1850 B			
605	1.04 ± 0.06	0.41 ± 0.03	0.54 ± 0.04	0.40 ± 0.04	0.38	0.09
1020	0.69 ± 0.03	0.27 ± 0.01	0.62 ± 0.03	...	0.36	0.07
1077	1.02 ± 0.08	...	0.55 ± 0.03	0.34 ± 0.04	0.33	0.08
1146	0.60 ± 0.02	0.24 ± 0.01	0.63 ± 0.04	0.43 ± 0.02	0.34	0.07
1153	0.42 ± 0.02	0.23 ± 0.01	0.62 ± 0.07	0.54 ± 0.03	0.34	0.11
1160	0.67 ± 0.02	0.24 ± 0.02	0.61 ± 0.02	0.41 ± 0.02	0.35	0.05
1161	0.67 ± 0.01	0.25 ± 0.01	0.63 ± 0.015	0.41 ± 0.02	0.37	0.07

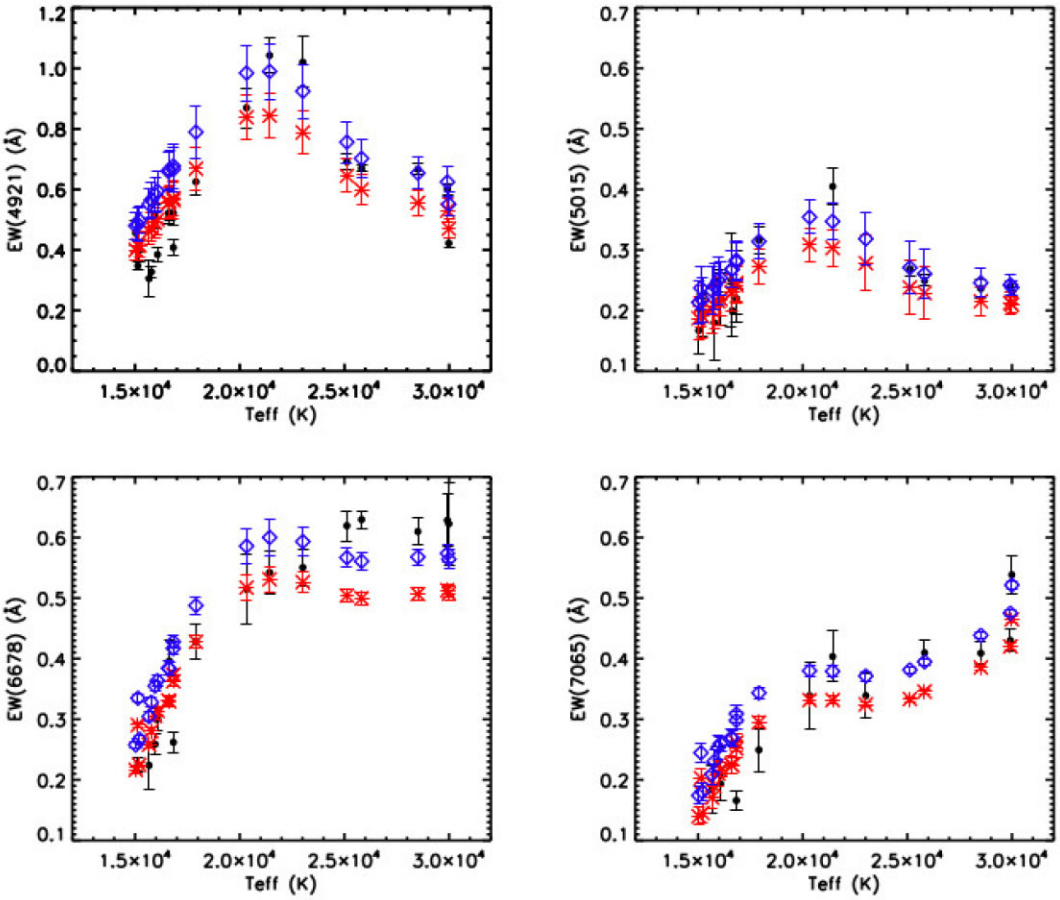

Figure 5. Equivalent width (Å) for each line obtained from MUSE spectra (black dots) and from the interpolation of the theoretical EWs with different He mass fractions: red asterisks and blue diamonds for models with $Y = 0.25$ and $Y = 0.35$, respectively.

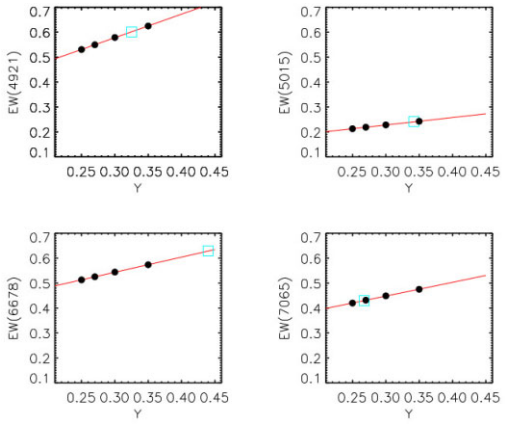

Figure 6. Values of the EW_{obs} (cyan square) and the EW_{th} (black circles) corresponding to $Y = 0.25$, 0.27, 0.30, and 0.35, for star #1146. The red lines represent the linear fits of the synthetic data.

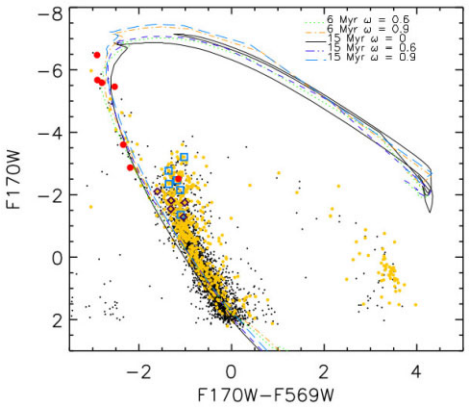

Figure 7. (F170W – F569W, F170W) CMD of NGC 1850 with superimposed isochrones with different rotation rates and ages from Marigo et al. (2008) and Nguyen et al. (2022). Isochrones are colour-coded, in terms of their Ω/Ω_{cr} and age, as follows: $\Omega/\Omega_{cr} = 0$ at age 15 Myr, black line; $\Omega/\Omega_{cr} = 0.6$ at 15 Myr, purple dashed line; $\Omega/\Omega_{cr} = 0.9$ at 15 Myr, dark green long-dashed line; $\Omega/\Omega_{cr} = 0.6$ at 6 Myr, green dotted line; $\Omega/\Omega_{cr} = 0.9$ at 6 Myr, cyan dash–dotted line. Targets associated with stars that are He-enhanced are marked by red circles.

We note that four stars of this subsample are located at a distance from the centre of NGC 1850 B less than 5 arcmin, namely #1146, #1153, #1160, and #1161. The other three are at a larger apparent distance from the centre; however, a quick check by eye shows that they seem to lie on the edge between the two subclusters.

We find that some of the He-rich stars are in common with the weak-O targets found by Sollima et al. (2022). If confirmed, this could be extremely interesting just because this kind of anticorrelation is typical of multipopulations in GGCs, in which the second generations of stars are rich in He and poor in O. However, we remark that the two samples of stars (He-normal and He-rich) do not overlap in effective temperature, thus hampering a direct comparison and possibly leading to unknown sources of systematic error.

4.3 Uncertainties

The internal uncertainties on our He abundances include errors due to the determination of atmospheric parameters. We evaluated the effective temperature and gravity of the B stars by comparing with theoretical models having the same colour and magnitude of stars as in our sample. The uncertainties on these quantities are dominated by the uncertainties on the magnitudes and distance. The photometric error of our data is about 0.02 mag (Gilmozzi et al. 1994). At the typical temperature of our sample, this translates to an uncertainty in temperature of ∼1000 K and in gravity of ∼0.01 dex. To estimate the internal uncertainties associated with the He contents, we recomputed the abundance for a set of B stars, varying the initial atmospheric parameters by (adding/subtracting) a quantity equal to their expected errors. By summing in quadrature the two contributions, we estimate the total uncertainty in Y to be as large as 0.04, dominated by errors from temperature. Except for a few stars, this evaluation of uncertainty appears smaller than the σ values estimated with the procedure of measuring the He abundance (see Table 2).

A systematic error on the estimation of the atmospheric parameters could be due to the use of different grid models with respect to the TLUSTY ones to convert the theoretical isochrones to the WFPC2 photometric system. In fact, Marigo and collaborators used the transformations primarily based on the LTE ATLAS9 (Castelli & Kurucz 2003) synthetic atmospheric models.

On this matter, we note that the LTE ATLAS9 and non-LTE TLUSTY model atmospheres both assume the same microturbulence,[3] namely 2 km s^{-1}. Furthermore, Przybilla, Nieva & Butler (2011) tested the LTE ATLAS9 and non-LTE TLUSTY model atmospheres, concentrating their work on early-type stars of effective temperature between 15 000 and 35 000 K. They found that the temperature structures of the two models are in agreement: the differences are at most 1–2 per cent and they are even smaller for low metallicity. As a result of this work, they concluded that such a small difference is irrelevant for stellar parameter determination. Moreover, Lanz & Hubeny (2007) compared the same model atmospheres for B stars. These authors found negligible differences between the continuum of the two spectra sets. The strongest difference is in the near-ultraviolet range, where the LTE fluxes are about 10 per cent higher than the non-LTE predictions. This leads to a difference in the estimation of the effective temperature using *HST* broad bands lower than the uncertainties reported in our paper. We conclude that the use of the ATLAS9 models instead of TLUSTY ones does not affect the results of this work.

The possible systematic errors on the atmospheric parameters due to the uncertainties in the adopted reddening have been also evaluated. For this purpose, we recomputed the temperature and gravity of each star by varying the initial reddening in an artificial way, namely by adding/subtracting to the original reddening of a quantity equal to their expected errors (0.015) (Górski et al. 2020). As a result, we obtained mean differences in effective temperature of about 200 K and in log g of about 0.01 dex; both values are well within the uncertainties considered in this work.

Another source of systematic uncertainty that could affect the He abundance is the microturbulence. Microturbulence is sensitive to stellar atmospheric parameters, especially surface gravity (Hunter et al. 2007). By analysing the spectra of 102 B stars, Lyubimkov, Rostopchin & Lambert (2004) found that stars with mass between ∼4 and 7 $M_\odot$ have a microturbulence velocity (V_t) between 0 and 5 km s^{-1}, with an average of about 1.7 km s^{-1}, while stars with mass in the range of 7–11 $M_\odot$ have the same spread and average value of microturbulence as the previous case until their relative age t/t_{MS} is less then 0.8. After this value, the microturbulence velocity could

[3] https://wwwuser.oats.inaf.it/fiorella.castelli/grids.html.

increase to ∼11 km s^{-1}, with an average of about 7 km s^{-1}. For the most massive stars (12–18 $M_\odot$), the microturbulence velocity ranges between 4 and 23 km s^{-1} and depends on the relative age t/t_{MS}.

Recently, Liu et al. (2022) found an empirical relationship between the microturbulence and surface gravity for B-type stars:

$$V_{armt} = -3.97(\log g)^2 + 17.85(\log g) - 2.52.$$

The choice of 2 km s^{-1} for our theoretical models is in agreement with the quoted studies, but for the hottest and massive ones, #1146, #1153, #1160, #11161, a more accurate V_t should be about 7 km s^{-1}. We believe that microturbulence may play a role in constraining the He abundance in young hot stars, such as those we study here. Nevertheless, it does not seem that uncertainties in microturbulence can have an impact so severe as to generate the He enhancement we found here.

4.4 Rotation

Because stellar rotation contributes to the broadening of line profiles in stellar spectra, in this section we discuss its possible role in the EW values of He lines in NGC1850 B star spectra. The aim is to understand if the increase of EW_{obs} associated with the He line profiles is due to rotation or to the He-enhancement. Because the resolution of MUSE spectra is not high enough to analyse the issue in detail, we provide a qualitative analysis.

To find a plausible rotation velocity of the B stars of NGC1850 B, we compared the CMD with the isochrones of rotating models obtained from PARSEC version 2.0 (Nguyen et al. 2022). As an input indication for the age of these models, we took into account the work by Sollima et al. (2022) and Fischer, Welch & Mateo (1993), which fitted the CMD of NGC 1850 B with a non-rotating isochrone of 15 and 6 Myr, respectively. Thus, we compared the *HST* photometry to five isochrones at 6 and 15 Myr computed with different rotation rates $\omega = \Omega/\Omega_{cr} = 0$, 0.6, and 0.9, where Ω is the angular velocity and Ω_{cr} is the breakup velocity; that is, the angular velocity at which the centrifugal force is equal to the effective gravity at the equator. As shown in Fig. 7, the CMD of NGC 1850 B is well fitted by all the isochrones taken into account, both rotating and non-rotating. By adopting these theoretical models, the stars having F170W ∼ –6 are reproduced by isochrones of 6 and 15 Myr and $\omega = 0.6$, giving an equatorial velocity $v_{eq} \simeq$ 230–250 km s^{-1}. On the other hand, if the isochrones with $\omega = 0.9$ are adopted, an equatorial velocity of $v_{eq} \simeq$ 410 km s^{-1} is found.

Because velocities of 230–250 km s^{-1} are derived for some stars of NGC 1850 B in the analysis by Kamann et al. (2023) and by Sollima et al. (2022), we decided to compute the theoretical spectra with ROTIN by assuming $Y = 0.25$ and a rotation velocity of 250 km s^{-1}. Also in this case, the synthetic spectra were degraded to the MUSE resolution and normalized. We considered the same set of T_{eff} and $\log g$ of the grid *BSTAR2006*. The procedure detailed in Section 3 was used to derive the EW_{th} of these models for each He line. Because we are taking into account the case of Ω/Ω_{cr} =0.6, the effect of the rotation on the atmospheric parameters can be neglected (Frémat et al. 2005).

As an indicator of the quality of the derived EW_{th}, we determined the mean value of the difference Δ_{EWrot} between the EW_{th} evaluated from the synthetic models with rotation ($V\sin i = 250$ km s^{-1}) and the observed ones. In this analysis we excluded the He-weak stars. The following results were obtained:

(i) $\Delta_{EWrot} = 0.04 \pm 0.04$ for NGC 1850 A;
(ii) $\Delta_{EWrot} = 0.03 \pm 0.05$ for NGC 1850 B.

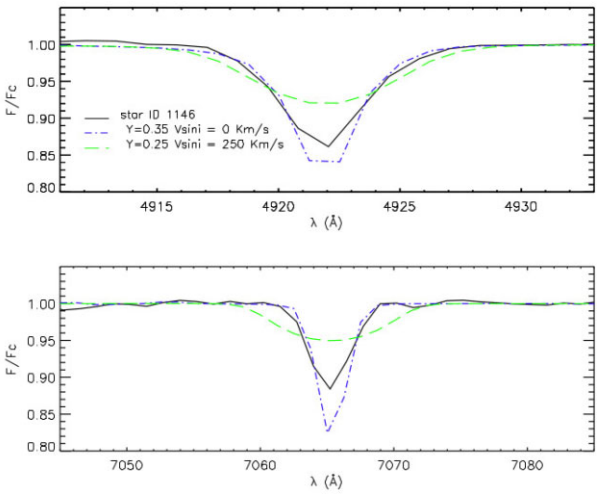

Figure 8. Spectra of star #1146 (black line), in the range of wavelength around the He lines at ∼4922 and 7065 Å. They are compared with the synthetic spectra calculated with $Y = 0.35$ and $V\sin i = 0$ km s^{-1} (blue dot–dashed line), and with $Y = 0.25$ and $V\sin i = 250$ km s^{-1} (green dashed line).

In a similar way and including the same stars, we derived the mean difference between the EW_{th} estimated from the models with $V\sin i = 0$ but Y different ($Y = 0.25$ for the normal stars, $Y = 0.35$ for the He-enhanced stars, and $Y = 0.27$ for #1069) and the observed ones. In this case, we found the following values:

(i) $\Delta_{EW} = 0.0007 \pm 0.03$ for NGC 1850 A;
(ii) $\Delta_{EW} = 0.002 \pm 0.050$ for NGC 1850 B.

The comparison of the values of this indicator ($\Delta_{EW} << \Delta_{EWrot}$) shows that the synthetic models without rotation provide a fit of the observed EWs of much better quality than the synthetic models with rotation. This can also be appreciated by eye in Fig. 8, where we show the spectra of the NGC 1850 B star #1146 (black line) in the range of wavelength around two He I lines at 4922 Å (upper panel) and 7065 Å (lower panel). The two synthetic spectra are also plotted; they represent the results of the models with rotation and $Y = 0.25$ (green dashed line), and without rotation but $Y = 0.35$ (blue dot–dashed line). From this plot, it is evident that the model with rotation does not reproduce the wings and the depth of the He lines. Instead, the He-enriched models fit the wings of the lines well,but are too deep. It is important to recall here that the resolution of the MUSE spectra is quite low and prevents a strong conclusion. A further intriguing possibility that could be confirmed or rejected by the analysis of high-resolution spectra is briefly as follows. Because fast rotation induces turbulent diffusion in the stellar interior, which drives the CNO-cycled material from the core to the envelope (Meynet & Maeder 2000), a possible hypothesis could be an He-enhancement (less than 0.35 in mass fraction) due to stellar rotation (less than 250 km s^{-1}).

5 CONCLUSIONS

In this paper we have examined for the first time the He abundance of B stars in the young (∼90 Myr) binary LMC cluster NGC 1850. This system could be a unique bridge between two young massive stellar clusters observed during their process of formation of a multiple population and the old GCs exhibiting multiple populations.

We analysed the spectra of 20 B stars extracted by MUSE cubes. To determine the He abundance, we compared the EWs of four He

lines (4922, 5015, 6678, and 7065 Å) calculated from the MUSE spectra with those found by analysing the theoretical spectra.

These spectra were computed with the code SYNSPEC, using non-LTE line-blanketed model atmospheres of the grid *BSTARS*2006 for early B stars (Lanz & Hubeny 2007). We computed the model considering four He mass fraction: 0.25, 0.27, 0.30, 0.35.

The results can be summarized as follows.

(i) We found a non-homogeneous He abundance. In particular, we can divide the targets of our sample into three groups: He-normal ($Y = 0.25 \pm 0.01$), He-weak ($Y < 0.24$), and He-rich ($Y > 0.26$).

(ii) The last group is intriguing because all stars except one belong to the young isochrone, at 15 Myr; four of them are at a distance of less then 5 arcmin from the centre of NGC 1850 B, and the others are at the edge between the two clusters. The mean value of the He mass fraction is about 0.35 ± 0.02.

(iii) Some He-rich stars are in common with the weak-O stars found by Sollima et al. (2022). If this is confirmed, for example through the analysis of high-resolution spectroscopy, it will be the first proof of anticorrelation in massive clusters younger than 2 Gyr in the MCs .

(iv) The He-normal and He-weak stars are associated with the isochrone at 90 Myr.

(v) We evaluated the effect of rotation on the He abundance by computing synthetic spectra with $Y = 0.25$ and $V\sin i = 250$ km s^{-1}, in agreement with the works of Kamann et al. (2023) and with the $v_{\rm eq}$ values of the best isochrone that fits the CMD. From our qualitative analysis, the models without rotation but different Y fit the observed EWs of NGC1850 B stars better, but the resolution of the MUSE spectra is too low to reach a strong conclusion.

(vi) We highlight that unfortunately our sample of He-normal and He-rich stars do not overlap in effective temperature, thus hampering the quantification of possible sources of systematic errors.

In order to gain a deeper understanding of the characteristics or properties of the He features and clarify their nature, it is essential to perform high-resolution spectroscopic analyses (on which we will focus in future observational campaigns).

ACKNOWLEDGEMENTS

RC thanks Antonio Sollima, dearest friend, colleague, and creator of this work. Sadly, he passed away prematurely, before seeing the final results. She thanks him for his advice and support, but even more for his friendship, joy, humour, music, and chats. She will be forever grateful to have had the opportunity to work together and to spend part of her life in his company.

This work is based on observations collected at the European Organisation for Astronomical Research in the Southern Hemisphere under ESO program 0102.D-0268(A) and made with the NASA/ESA *Hubble Space Telescope* and obtained from the Hubble Legacy Archive, which is a collaboration between the Space Telescope Science Institute (STScI/NASA), the Space Telescope European Coordinating Facility (ST-ECF/ESA), and the Canadian Astronomy Data Centre (CADC/NRC/CSA).

We thank the anonymous referee for the valuable comments and suggestions that improved the quality of the publication.

DATA AVAILABILITY

The data underlying this article will be shared on reasonable request to the corresponding author.

REFERENCES

Asplund M., Grevesse N., Sauval A. J., 2005, in Barnes T. G.I., Bash F. N.eds, ASP Conf. Ser. Vol. 336, Cosmic Abundances as Records of Stellar Evolution and Nucleosynthesis. Astron. Soc. Pac., San Francisco, p. 25
Auer L. H., Mihalas D., 1973, ApJS, 25, 433
Bacon R. et al., 2010, in McLean I. S., Ramsay S. K., Takami H.eds, Soc. Photo-Optical Instrum. Eng. (SPIE) Conf. Ser. Vol. 7735, Ground-based and Airborne Instrumentation for Astronomy III. SPIE, Bellingham, p. 773508
Barnard A. J., Cooper J., Smith E. W., 1974, J. Quant. Spec. Radiat. Transf., 14, 1025
Bastian N., Lardo C., 2018, ARA&A, 56, 83
Bastian N., de Mink S. E., 2009, MNRAS, 398, L11
Bastian N. et al., 2016, MNRAS, 460, L20
Bastian N. et al., 2017, MNRAS, 465, 4795
Baumgardt H., Hilker M., 2018, MNRAS, 478, 1520
Carini R., Biazzo K., Brocato E., Pulone L., Pasquini L., 2020, AJ, 159, 152
Cassisi S., Salaris M., Pietrinferni A., Hyder D., 2017, MNRAS, 464, 2341
Castelli F., Kurucz R. L., 2003, in Piskunov N., Weiss W. W., Gray D. F.eds, Proc. IAU Symp. Modelling of Stellar Atmospheres. Vol. 210, Published on behalf of the IAU by the Astronomical Society of the Pacific, Uppsala, Sweden, p. A20
Chantereau W., Charbonnel C., Meynet G., 2016, A&A, 592, A111
Correnti M., Goudfrooij P., Bellini A., Kalirai J. S., Puzia T. H., 2017, MNRAS, 467, 3628
Costa G., Girardi L., Bressan A., Chen Y., Goudfrooij P., Marigo P., Rodrigues T. S., Lanza A., 2019, A&A, 631, A128
D'Antona F., Caloi V., 2004, ApJ, 611, 871
D'Antona F., Di Criscienzo M., Decressin T., Milone A. P., Vesperini E., Ventura P., 2015, MNRAS, 453, 2637
Doherty C. L., Gil-Pons P., Lau H. H. B., Lattanzio J. C., Siess L., Campbell S. W., 2014, MNRAS, 441, 582
Dolphin A. E., 2000, PASP, 112, 1383
El-Badry K., Burdge K. B., 2022, MNRAS, 511, 24
Fischer P., Welch D. L., Mateo M., 1993, AJ, 105, 938
Frémat Y., Zorec J., Hubert A. M., Floquet M., 2005, A&A, 440, 305
Garrison R. F., Gray R. O., 1994, AJ, 107, 1556
Gilmozzi R., Kinney E. K., Ewald S. P., Panagia N., Romaniello M., 1994, ApJ, 435, L43
Górski M. et al., 2020, ApJ, 889, 179
Goudfrooij P., Girardi L., Correnti M., 2017, ApJ, 846, 22
Gratton R., Bragaglia A., Carretta E., D'Orazi V., Lucatello S., Sollima A., 2019, A&A Rev., 27, 8
Hubeny I., Lanz T., 2017a, preprint (arXiv:1706.01859)
Hubeny I., Lanz T., 2017b, preprint (arXiv:1706.01937)
Hubeny I., Allende Prieto C., Osorio Y., Lanz T., 2021, preprint (arXiv:2104.02829)
Hunter I. et al., 2007, A&A, 466, 277
Kamann S., Bastian N., Usher C., Cabrera-Ziri I., Saracino S., 2021, MNRAS, 508, 2302
Kamann S. et al., 2023, MNRAS, 518, 1505
Keller S. C., Mackey A. D., Da Costa G. S., 2011, ApJ, 731, 22
Kelz A., Kamann S., Urrutia T., Weilbacher P., Bacon R., 2016, in Skillen I., Balcells M., Trager S.eds, ASP Conf. Ser. Vol. 507, Multi-Object Spectroscopy in the Next Decade: Big Questions, Large Surveys, and Wide Fields. p. 323
Lagioia E. P., Milone A. P., Marino A. F., Dotter A., 2019, ApJ, 871, 140
Lanz T., Hubeny I., 2007, ApJS, 169, 83
Leckrone D. S., 1971, A&A, 11, 387
Li C. et al., 2023, ApJ, 948, 8
Liu Z., Cui W., Liu C., Alexeeva S., Shi J., Zhao G., 2022, ApJ, 937, 110
Lyubimkov L. S., Rostopchin S. I., Lambert D. L., 2004, MNRAS, 351, 745
Mackey A. D., Broby Nielsen P., Ferguson A. M. N., Richardson J. C., 2008, ApJ, 681, L17
Marigo P., Girardi L., Bressan A., Groenewegen M. A. T., Silva L., Granato G. L., 2008, A&A, 482, 883

Marino A. F. et al., 2014, MNRAS, 437, 1609
Meynet G., Maeder A., 2000, A&A, 361, 101
Milone A. P., 2015, MNRAS, 446, 1672
Milone A. P., Marino A. F., 2022, Universe, 8, 359
Milone A. P. et al., 2017, MNRAS, 465, 4363
Milone A. P. et al., 2018, MNRAS, 477, 2640
Milone A. P. et al., 2020, MNRAS, 492, 5457
Milone A. P. et al., 2023, A&A, 672, A161
Molnar M. R., 1972, ApJ, 175, 453
Mucciarelli A., Dalessandro E., Ferraro F. R., Origlia L., Lanzoni B., 2014, ApJ, 793, L6
Nguyen C. T. et al., 2022, A&A, 665, A126
Niederhofer F., Hilker M., Bastian N., Silva-Villa E., 2015, A&A, 575, A62
Osawa K., 1965, Ann. Tokyo Astron. Obser., 9, 121
Przybilla N., Butler K., Heber U., Jeffery C. S., 2005, A&A, 443, L25
Przybilla N., Nieva M. F., Heber U., Jeffery C. S., 2006, Baltic Astron., 15, 163
Przybilla N., Nieva M.-F., Butler K., 2011, in J. Phys. Conf. Ser., p. 012015, preprint (arXiv:1111.1445),
Saracino S. et al., 2022, MNRAS, 511, 2914
Shamey L. J., 1969, PhD thesis, Univ. Colorado
Siess L., 2010, A&A, 512, A10
Sollima A., D'Orazi V., Gratton R., Carini R., Carretta E., Bragaglia A., Lucatello S., 2022, A&A, 661, A69
Song Y.-Y., Mateo M., Bailey J. I., Walker M. G., Roederer I. U., Olszewski E. W., Reiter M., Kremin A., 2021, MNRAS, 504, 4160
Vallenari A., Aparicio A., Fagotto F., Chiosi C., Ortolani S., Meylan G., 1994, A&A, 284, 447
Van der Swaelmen M., Hill V., Primas F., Cole A. A., 2013, A&A, 560, A44
Wolff S. C., Heasley J. N., 1985, ApJ, 292, 589

This paper has been typeset from a TEX/LATEX file prepared by the author.